



## Detection of masses in mammogram images using CNN, geostatistic functions and SVM

Wener Borges Sampaio<sup>a</sup>, Edgar Moraes Diniz<sup>a</sup>, Aristófanês Corrêa Silva<sup>a,\*</sup>,  
Anselmo Cardoso de Paiva<sup>a</sup>, Marcelo Gattass<sup>b</sup>

<sup>a</sup> Federal University of Maranhão – UFMA, Applied Computing Group – NCA, Av. dos Portugueses, SN, Campus do Bacanga, Bacanga 65085-580, São Luís, MA, Brazil

<sup>b</sup> Pontifical Catholic University of Rio de Janeiro – PUC-Rio, R. São Vicente, 225 Gávea, 22453-900 Rio de Janeiro, RJ, Brazil

### ARTICLE INFO

#### Article history:

Received 11 May 2010

Accepted 30 May 2011

#### Keywords:

Mammogram

Computer-aided detection

Cellular neural networks

Geostatistical functions

Support vector machines

### ABSTRACT

Breast cancer occurs with high frequency among the world's population and its effects impact the patients' perception of their own sexuality and their very personal image. This work presents a computational methodology that helps specialists detect breast masses in mammogram images. The first stage of the methodology aims to improve the mammogram image. This stage consists in removing objects outside the breast, reducing noise and highlighting the internal structures of the breast. Next, cellular neural networks are used to segment the regions that might contain masses. These regions have their shapes analyzed through shape descriptors (eccentricity, circularity, density, circular disproportion and circular density) and their textures analyzed through geostatistic functions (Ripley's  $K$  function and Moran's and Geary's indexes). Support vector machines are used to classify the candidate regions as masses or non-masses, with sensitivity of 80%, rates of 0.84 false positives per image and 0.2 false negatives per image, and an area under the ROC curve of 0.87.

© 2011 Elsevier Ltd. Open access under the [Elsevier OA license](http://www.elsevier.com/locate/elsevier).

### 1. Introduction

Statistics indicate an increase in the frequency of breast cancer in developed countries as much as in emergent ones. According to the World Health Organization (WHO), in the 1960's and 1970's a ten-fold increase was registered in the incidence rates, adjusted by age, in the cancer records of several countries [1].

In the last decades, many research projects have been carried out aiming to develop computational systems to help specialists in the task of interpreting radiological images. These computer-aided detection (CAD) and diagnosis (CADx) systems have gained more and more space in modern medicine, providing specialists with a second source of information and increasing the success rates of the precocious identification of serious diseases, such as breast cancer [2]. The efficiency of CAD/CADx systems depends on the techniques applied for the segmentation and extraction of features.

This work presents a CAD methodology to help specialists in the task of detecting masses in mammogram images. The methodology uses cellular neural networks to segment the regions of interest, then extracts shape features from those regions and

describes their texture through Ripley's  $K$  function, Moran's and Geary's indexes. Finally, the supervised learning method support vector machine (SVM) is used to classify the candidate regions as masses or non-masses. In this context, we consider as mass any region that corresponds to a neoplasm, whether it is malignant or benign.

The main contributions of this paper are demonstrating the potential of cellular neural networks to segment suspect regions in mammographic images and proposing a methodology that includes an innovative use of geostatistical functions as texture signatures for mass detection. The quality of the results obtained by this work can allow this methodology to be added to a computer tool for the medical area, providing support to specialists especially in cases in which visualization is difficult.

This work is organized as follows. In Section 2 we present some related works. Section 3 presents the techniques for the extraction, classification and validation of features, as well as a detailed description about the proposed methodology and evaluation. Next, in Section 4, the results are shown and we discuss the application of the techniques under study. Finally, Section 5 presents some concluding remarks.

### 2. Related works

Many different methodologies have been proposed for tools that can assist in the precocious detection and diagnosis of cancer.

\* Corresponding author. Tel.: +55 98 33018243; fax: +55 98 33018841.

E-mail addresses: [wenersampaio@yahoo.com.br](mailto:wenersampaio@yahoo.com.br) (W. Borges Sampaio), [edgkff@gmail.com](mailto:edgkff@gmail.com) (E. Moraes Diniz), [ari@dee.ufma.br](mailto:ari@dee.ufma.br) (A. Corrêa Silva), [paiva@deinf.ufma.br](mailto:paiva@deinf.ufma.br) (A. Cardoso de Paiva), [mgattass@tecgraf.puc-rio.br](mailto:mgattass@tecgraf.puc-rio.br) (M. Gattass).

Several methods were proposed for mass detection (see for instance [3–9]). These works achieved sensitivity rates varying from 81% to 98%, and rates of false positives per image from 0.33 to 4.3. In general these works use subsets of the publicly available databases of mammographic images MIAS [10] and DDSM [11].

Cellular neural networks (CNNs) have been used in several applications for image processing [12] and signal processing in electroencephalograms [13,14]. The use of this technique for the classification of medical images (ultrasonic imaging, X-ray computed tomography, or magnetic resonance imaging) started with the works by Rekeczky et al. [15], Szabo et al. [16] and Arena et al. [17]. In order to test two features of breast cancer, CNNs were used by Chua et al. [18]. The first feature corresponds to microcalcifications and the second to structures with spiculated shape around a given tumor, indicating the presence of typical blood vessels.

Costa et al. [19] compared the efficiency of the support vector machine (SVM) to that of linear discriminant analysis (LDA), classifying 200 regions of interests (ROIs) – 50 malignant tissues, 50 benign tissues and 100 normal tissues – from mammogram images supplied by the MIAS database and 3600 regions of interest – 900 malignant tissues, 900 benign tissues and 1800 normal tissues – from the DDSM. The results of detection using MIAS achieved a performance of 85% and 97% for LDA and SVM, respectively. Using the DDSM, the authors achieved 89.2% and 99.6% for LDA and SVM, respectively. These results indicate that SVM achieves higher performance in the detection of masses in the images used.

Another interesting technique used is based on self-organizing maps. Oliveira et al. [20] proposed a technique using growing neural gas (GNG) for the segmentation of mass candidates, and SVM combined with Ripley's *K* function to detect masses in mammograms. The authors used 997 images from the DDSM, obtaining a sensitivity of 89.3%, 0.93 false positives per image and 0.02 false negatives per image.

Nunes et al. [21] proposed a methodology for the detection of masses that uses the *K*-means clustering algorithm and the template matching technique to segment the suspect regions. The methodology was tested with 650 mammographic images from the DDSM. The stage at which the suspect regions are segmented managed 603 masses in the sample, what means 92.77% of the cases, and also selected 2076 non-masses. Then, geometry and texture measurements are extracted from each suspect region, and the texture is described through Simpson's diversity index. Finally, this information is submitted to an SVM, to classify the suspect regions as masses or non-masses. The classification stage achieved an average accuracy of 83.94%, sensitivity of 83.24%, and 84.14% of specificity, with a rate of 0.55 false positives per image and 0.17 false negatives per image.

Wang et al. [8] proposed a new scheme for detection of masses in mammograms using pixel intensity features (contrast, invariant momentum, average, gradient, standard deviation and gradients of boundaries), geometry features (circularity, density, sphericity and Fourier descriptor) and texture descriptors (Law's template, co-occurrence matrix, Wavelet transform) to characterize suspect regions and SVM-RF (support vector machine with relevance feedback) to classify the regions of interest as masses or non-masses. The DDSM was used, being 192 images used for training and 150 for testing. This method achieved 90.6% of sensitivity and a rate of 3.6 false positives per image.

Pereira et al. [22] analyzes the performance of the random forest method for the detection of masses using information extracted through the ridgelet transform from craniocaudal and oblique mediolateral views separately and after grouped. The image database used was the DDSM, from which 270 regions of interest, containing masses and normal tissues, were selected.

This methodology achieved a performance of 94.4% of sensitivity, 96.9% of specificity and 91.8% of accuracy.

Therefore, one can verify the importance of detecting masses in the breast. This is sought through the use of several techniques of machine learning and an infinity of features are searched in order to improve the characterization of tissues and support the classification of these tissues as normal and masses. So, it seems to be very promising to investigate the application of cellular neural networks with a set of features that describe and characterize the geometry and the texture of the samples of breast tissue images.

### 3. Proposed method

This section describes the methodology proposed in this work to detect masses in digital mammogram images. This methodology comprises the following stages: acquisition, pre-processing, segmentation of regions of interest, feature extraction, feature selection, and classification of the regions of interest as mass or non-mass. Fig. 1 presents a diagram illustrating these stages.

Acquisition is the first stage of any CAD tool. The following stage is pre-processing. This stage eases the processing to be performed by the subsequent stages by removing unwanted objects through the *K*-means algorithm, Canny's filter, Hough's transform and the erosion operator, and by enhancing the contrast of the image through histogram equalization.

The segmentation of regions of interest uses CNN to identify areas in the image that are suspect of containing masses, so that the following stages only work with relevant regions.

The feature extraction stage describes the regions of interest by means of their shape (eccentricity, circularity, compactness, circular disproportion and circular density) and texture (Ripley's *K* function, Moran's and Geary's indexes) features.

Finally, the selection of features was done using stepwise selection method and the classification stage selects the areas that contain masses and discards those which contain non-masses through the SVM classifier.

#### 3.1. Acquisition

For the development of this methodology we used the digital database for screening mammography (DDSM) [11]. This public database is a joint effort of some American institutions (Massachusetts General Hospital, Wake Forest University and Washington University School of Medicine in St. Louis) and contains 2.620 cases, freely available on the Web. Each case includes two images of each breast (CC and MLO views), besides additional information about the exam (date of the study, patient's age, type of pathology, number of anomalies, etc.) and about the image (file name, film type, date of digitalization, digitizer type, sequence, pixels per line, bits per pixel, marks, etc.). All information contained on DDSM was supplied by specialists.

In this work we used 623 images of this image database. These images were randomly selected, and the only requirement was that each image should have just one mass.

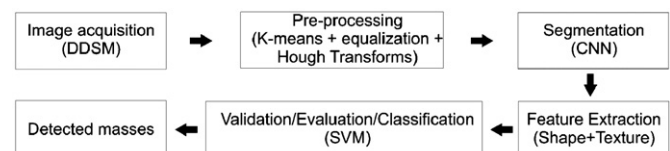


Fig. 1. Methodology stages.

### 3.2. Pre-processing

Images in the DDSM present noise and typical elements of the mammographic exam which can interfere with our methodology. These unwanted elements include patient identification or exam type marks, the background and occasionally noise produced by imperfections in the image generation or digitalization process. The objective of this pre-processing stage is to remove these unwanted elements in order to improve the discrimination of internal structures of the breast. Examples of these elements are illustrated in Fig. 2.

The pre-processing stage consists first in the reduction of the size of the original image, resulting in an image height of 1024

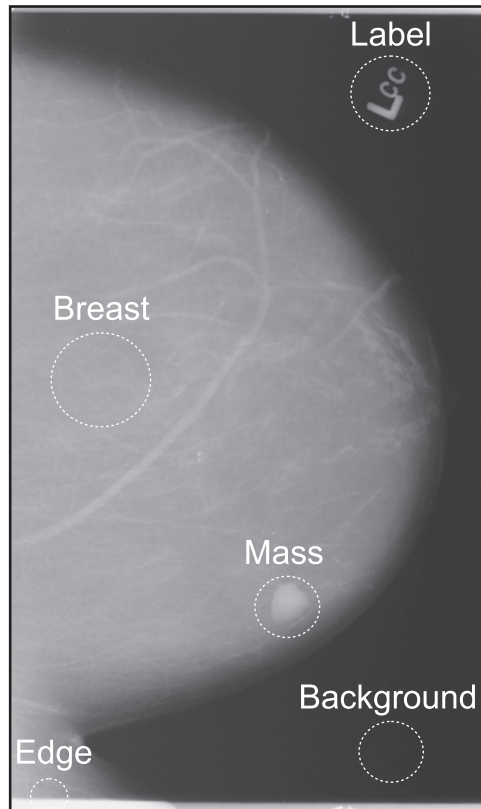


Fig. 2. Elements of an image from DDSM.

pixels and proportionally reducing the width (Fig. 3(a)). This reduction is needed to decrease the processing time, which would be very high otherwise. After the size reduction, all the points within 30 pixels from the lateral edges are removed, in order to eliminate the area between the radiography film edges and the empty spaces without film.

Next, the background, with gray levels close to black, is removed using the  $K$ -means algorithm [23], which clusters pixels into two groups ( $K=2$ ) according to their intensities (Fig. 3(b)). Thus, the pixels with higher intensities, such as those of the breast and those of the identification marks, are clustered into a group, while the pixels with lower intensity, such as those of the background and noise, are clustered into another group. Since the objective is to eliminate the lower-intensity group, the intensity values of those pixels are changed to zero (Fig. 3(c)).

In the resulting image (Fig. 3(c)) there are still external objects, such as exam identification labels or some noise. These objects are removed using the region-growing algorithm [24], which separates the disjoint regions in the image and generates a new image for each separated region (Fig. 4). Only the image whose object has the largest area, that is, the breast, is selected.

To end the pre-processing stage, we enhance the contrast of the image through histogram equalization. This improves the visualization of the internal breast structures (Fig. 5). Mediolateral oblique (MLO) view usually show chest muscle, which is associated to high gray levels. It interferes in the pixel intensity distribution and therefore may cause errors in the subsequent stages of the methodology. So, all images with MLO views are submitted to a new pre-processing stage for the removal of the chest muscle.

Initially we find the side where the chest muscle is located. This is done by dividing the image at half its width, and then calculating the average intensity of each half. The half with higher average is the one that contains the muscle. All the pixels below the middle of the image and in the opposite half are removed (Fig. 6(b)). Next, Canny's filter [25] is applied to detect the edges. Then, through the morphologic erosion operator, all detected edges which are in the same direction as the edge associated to the chest muscle are removed. All segments smaller than 5 pixels and larger than 15 pixels are removed as well (Fig. 6(c)), reducing the number of pixels and segments of the straight line to be analyzed. Next, using the Hough transform [25], we find the line that better represents the edge of the chest muscle (Fig. 6(d)). Finally, all the pixels from the image border to the straight line are removed (Fig. 6(e)).

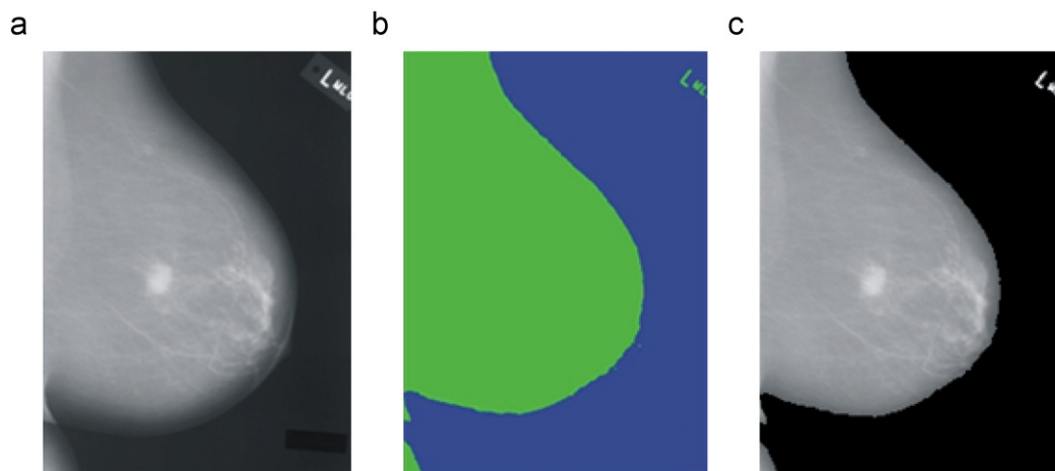


Fig. 3. Illustration of background removal. (a) Reduced image. (b) Image with edges removed and clustered by  $K$ -means ( $k=2$ ). (c) Image with background removed.

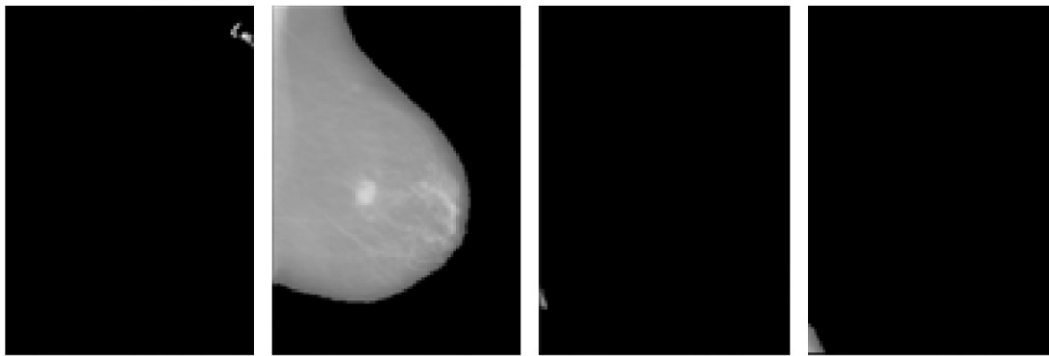


Fig. 4. Objects of Fig. 3(c) disjoint separated by the region growing algorithm.

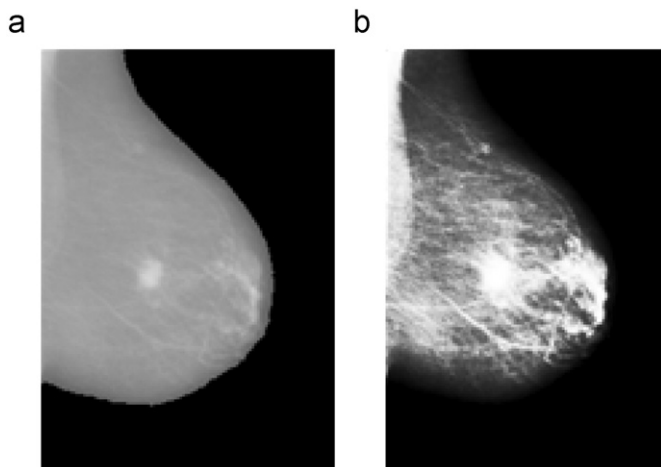


Fig. 5. Contrast enhancement through histogram equalization. (a) Image without enhancement. (b) Image with enhancement.

### 3.3. Segmentation

The segmentation stage aims to identify the breast regions with greater possibility of being masses. In this work, segmentation is performed through cellular neural networks [18].

According to Chua et al. [18], the standard architecture of a cellular neural network consists of a rectangular matrix with  $M \times N$  cells  $C(i,j)$  of Cartesian coordinates  $(i,j)$ , being  $i = 1, 2, 3, \dots, M$  and  $j = 1, 2, 3, \dots, N$ . Each cell is defined by:

$$\begin{cases} dx_{ij}(t) = -x_{ij}(t) + \sum_{C(k,l) \in S_r(i,j)} A_{i,j;k,l} y_{kl}(t) + \sum_{C(k,l) \in S_r(i,j)} B_{i,j;k,l} u_{kl} + z_{ij} \\ y_{ij} = \frac{1}{2} |x_{ij} + 1| - \frac{1}{2} |x_{ij} - 1| \end{cases} \quad (1)$$

where  $t$  is the time (iteration step) and  $S_r(i,j)$  is the sphere of influence of radius  $r$  ( $r \in \mathbb{N}_*^+$ ) of the cell  $C(i,j)$ , defined as the set of all neighboring cells  $(2r+1)(2r+1)$  with center in  $(i,j)$ .

The variables  $x_{ij}$ ,  $y_{kl}$ ,  $u_{kl}$  and  $z$  are called state, output image, input image and threshold of cell  $C(i,j)$ , respectively.  $A_{i,j;k,l}$  and  $B_{i,j;k,l}$  are the feedback operator and the synaptic input.

The input  $u_{kl}$  is the intensity of the pixels of an  $M \times N$  image in grayscale, normalized to the range of  $-1 \leq u_{kl} \leq +1$ , where white is coded as  $-1$  and black as  $+1$ .

Eq. (1) will be recomputed until there is no variation of state in any cell  $C(i,j)$  between the times  $t$  and  $t-1$ .

We used two templates to obtain the mass candidates. The first one is the Textudil [26] template, which is able to separate the mass candidates but has the collateral effect of inserting pixels that do not belong to the candidates. The second template,

Blur [26], does not insert extra pixels, but on the other hand might remove several pixels from the candidates.

The thresholds of the templates Textudil and Blur have been empirically established, and we used the values which achieved better performance, that is,  $Z = 4.5$  and  $1.0$ , respectively. Fig. 7 shows an example of segmentation using Textudil and Blur. After segmentation, all candidates smaller than  $15 \times 15$  pixels or larger than  $300 \times 300$  pixels are discarded. This way we prevent very small or very large candidates from passing to the subsequent stages. These values are based on previous studies by our research team [20].

Next, the images resulting from the segmentation using Textudil and Blur are aggregated using the binary OR operator. This aggregation aims to include candidates that were lost by one of the templates and to avoid repeated candidates. After this procedure, all candidates are separated through region growing, and those which do not meet the size criteria are eliminated, as shown in Fig. 8.

The image generated by the segmentation using CNN is binary. Nevertheless, since the following stages of the methodology use texture operators, we assign the pixel values of the equalized image to the segmented structures.

### 3.4. Features extraction

In this stage, the objective is to extract descriptive measurements from the regions of interest segmented in the previous stage, in order to generate feature vectors to be used in the classification stage. For that, shape and texture features are used.

The shape of the regions of interest used in this work is described through five features: eccentricity, circularity, compactness, circular disproportion and circular density. The procedure to extract these features does not take the intensity of the pixels in the regions of interest into account, just the shape of the segmented structures. Further details about these measurements can be found in [27] or in Appendix.

The texture of the regions of interest is described through Ripley's  $K$  function in the local form and in concentric rings [20], and through Moran's and Geary's indexes [28].

Ripley's  $K$  function, in its local form, is computed by choosing a center  $i$ , where the occurrence of pixels  $j$  with equal gray level, for different radius ( $r$ ) values, is examined.  $A$  is the area of the sample,  $n$  is the total number of points in the sample and  $\delta$  is a function that returns 1 if the distance  $d_{ij}$  between the points  $i$  and  $j$  is smaller than the radius  $r$ , or 0 otherwise:

$$K_i(r) = \frac{A}{n} \sum_{i \neq j} \delta(d_{ijr}) \quad (2)$$

Each gray level (spatial pattern) is analyzed separately from the others to determine whether an event occurs or not within the

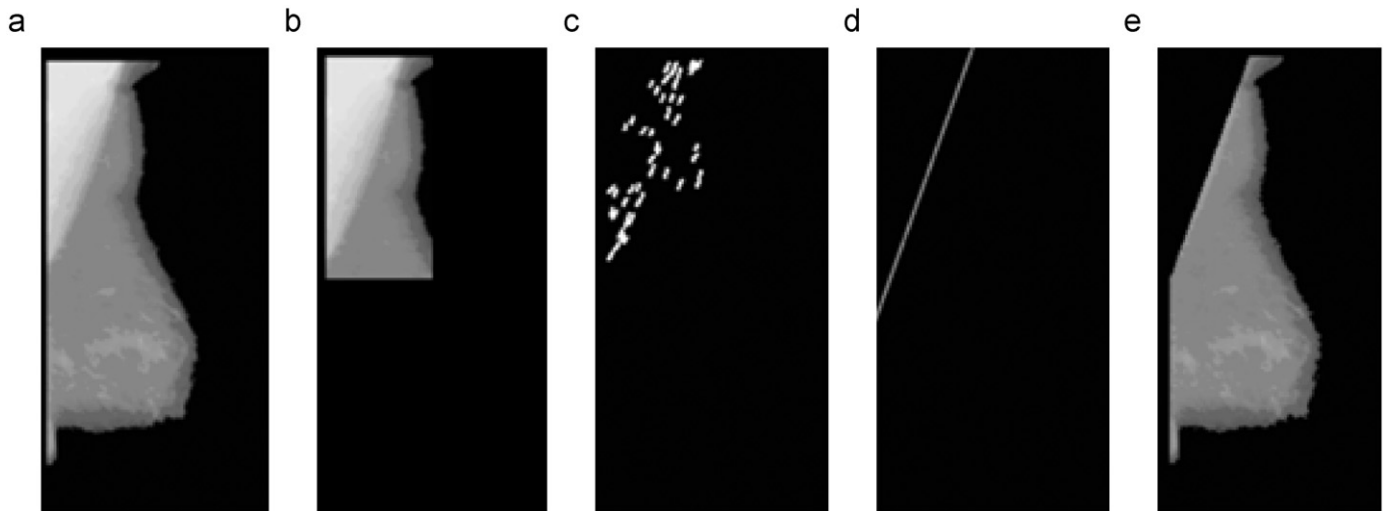


**Fig. 6.** Chest muscle removal. (a) MLO view. (b) Muscle area located. (c) Edges with same direction of the chest muscle located by Canny's filter and filtered by erosion. (d) Straight line detected by Hough transform. (e) Image without the chest muscle.

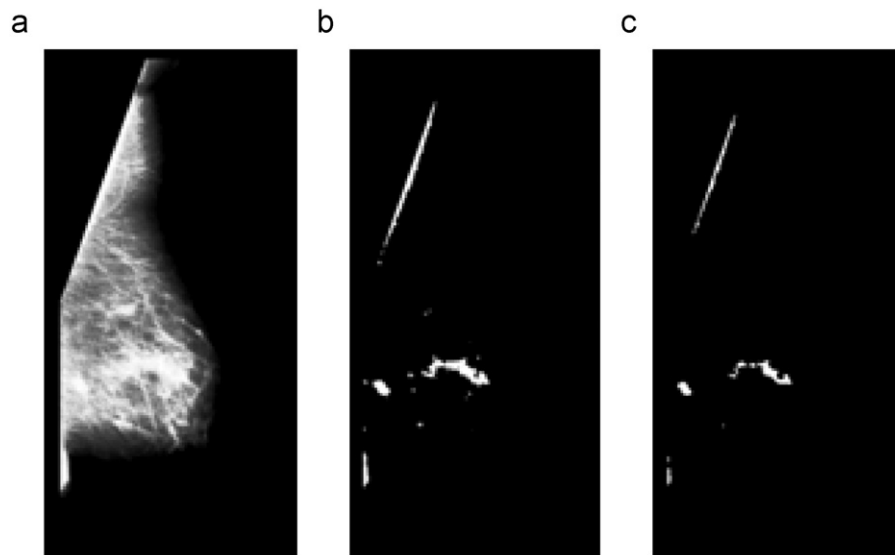


**Fig. 7.** Segmentation of a pre-processed image (a) through CNN using templates Textudil (b) and Blur (c).

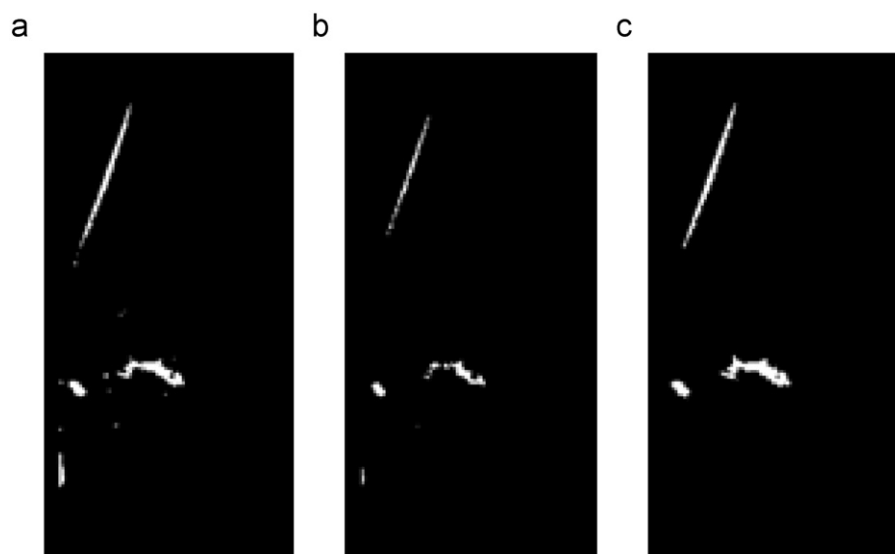


**Fig. 8.** (a) Objects selected by Textudil. (b) Objects selected by Blur. (c) Aggregated and filtered objects.



specified distance  $r$ . Thus, the number of elements in the feature vector obtained through  $K(r)$  is given by the number of gray levels present in the image multiplied by the desired number of radii.

For the analysis using Ripley's  $K$  function as described by Oliveira et al. [20], first we calculate the center of mass of each candidate. Next, we find the largest possible radius ( $R$ ) that starts in the center of mass of the candidate and goes to the most distant point of its border. This analysis is performed in two regions. The first corresponds to the circle (internal area) with the same center of mass as the candidate and radius  $r=R/2$ . The second region corresponds to the ring that has its external edge at a distance  $R$  from the center of mass of the candidate and internal edge at a distance  $r$  from that center (Fig. 9).

We also analyze the textures through Moran's and Geary's indexes, which calculate the spatial autocorrelation of a sample. In other words, they estimate to what extent the value of an attribute, observed in a region, depends on the values of that same attribute at neighbor locations.

To calculate these two indexes, first it is necessary to compute the proximity matrix ( $w$ ), which is a binary matrix where 1 is associated with zones that share the same boundary, and 0 are zones without this property. For convenience, this matrix is often normalized by line, that is, the sum of the weights of each line equals 1.

Moran's index ( $I$ ) is described by:

$$I = \frac{n}{W} \left( \frac{\sum_i \sum_j w_{ij} z_i z_j}{\sum_i z_i^2} \right) \quad \text{for } i \neq j \quad (3)$$

where  $n$  is the number of observations,  $w_{ij}$  is the element in the proximity matrix for the pair  $i$  and  $j$ ,  $W$  is the sum of the weights of the proximity matrix,  $z_i$  and  $z_j$  are the deviations in relation to the average, that is,  $z_i = x_i - \bar{x}$  and  $z_j = x_j - \bar{x}$ .

Geary's index ( $G$ ) is given by:

$$G = \frac{(n-1) \sum_{i=1}^n \sum_{j=1}^n w_{ij} (x_i - x_j)^2}{2(\sum_{i=1}^n \sum_{j=1}^n w_{ij}) \sum_{i=1}^n z_i^2} \quad \text{for } i \neq j \quad (4)$$

where  $x_i$  and  $x_j$  are the values of the variable of interest in the areas  $i$  and  $j$ ,  $\bar{x}$  is the average of the variables of interest in all areas of the sample,  $n$  is the number of areas in the sample, and  $w_{ij}$  is the element belonging to the proximity  $w$  and  $z_i = x_i - \bar{x}$ .

To calculate Moran's and Geary's indexes, we used a neighborhood ranging from 1 to 10 pixels, considering four directions that correspond to the angles  $0^\circ$ ,  $45^\circ$ ,  $90^\circ$  and  $135^\circ$ . These parameters were defined taking into account that the traditional analysis of Moran's and Geary's indexes can be computationally unfeasible for images where the candidates have larger areas. Such modification

allows a local analysis per pixel and significantly reduces the processing time.

It is important to stress that, for each type of texture descriptor, we use several levels of image quantization. In this study we have used 256, 128, 64, 32, 16 and 8 gray levels for each mass candidate. These quantizations aim to increase the possibility of texture relationships.

At the end of the feature extraction process, each region of interest is represented by a vector containing shape and texture information. More precisely, there are five features based on the sample's shape; Ripley's  $K$  function with  $(256+128+64+32+16+8)$  quantizations, where each quantization level produces the same number of features, totaling  $504 \text{ features} \times 2 \text{ rings} = 1008 \text{ features}$ ; Moran's index with  $(256+128+64+32+16+8)$  quantizations  $\times 4 \text{ directions} \times 10 \text{ neighborhoods} = 240 \text{ features}$ ; and Geary's index with  $(256+128+64+32+16+8)$  quantizations  $\times 4 \text{ directions} \times 10 \text{ neighborhoods} = 240 \text{ features}$ .

Further details about the application of Ripley's  $K$  function, Moran's and Geary's indexes applied to mammograms can be found in [27].

### 3.5. Classification

In the classification stage, the dataset is divided into two sets: training and test. In this work we used the leave-N-out cross-validation technique [29], because it does not depend on the proportion of the division between training and test.

First, the sample is separated in two groups: masses and non-masses. Next, each group is randomly divided into 10 subsets, from which one subset is chosen for training and the remaining ones are used for test. This process is repeated until all subsets have been tested.

In this work, the support vector machine (SVM) [29] was used with radial kernel and standard parameters ( $C=1$  and  $\gamma=0.5$ ).

Since the proportion of non-masses selected in the segmentation stage is approximately six times higher than the number of masses, we assigned a higher weight to the training of masses. This means that in training, the penalty for a mass classification error is greater than for a non-mass. A good balance between these two indexes was achieved using weight 9 for the mass sample and weight 1 for the non-mass sample.

We analyzed the classification performance by using the complete set of features and we applying stepwise selection method [29] for reducing and selection of features. The selection of features was done using the complete set of samples, and the leave-N-out process is done independently of this process.

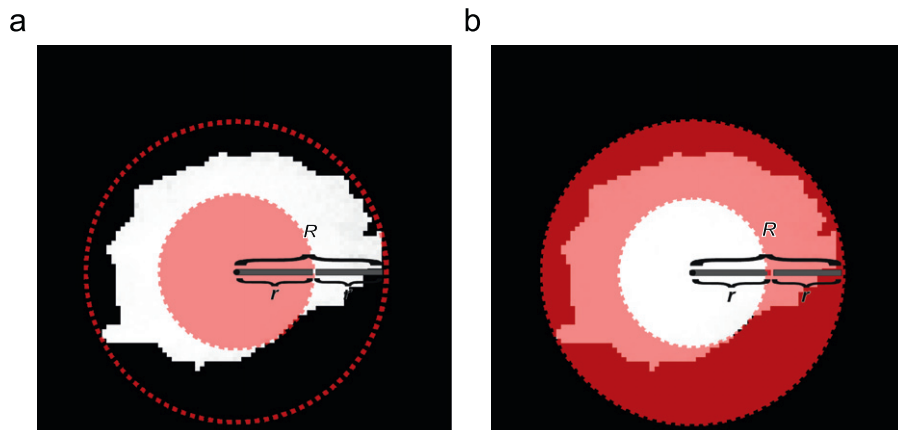


Fig. 9. Example of the use of Ripley's  $K$  function on a mass candidate.

### 3.6. Metrics and performance

In image processing and pattern recognition problems related to the medical area, the methodology performance is usually measured by calculating certain statistics about the results of the tests [30].

Given a sample with positive and negative cases of a certain pathology, the results of the classification tests for the analyzed cases can be divided into four groups: true positives (TP), false negatives (FN), true negatives (TN) and false positives (FP).

These numbers are used to generate measurements capable of quantifying the performance of a methodology, to evaluate how efficient it is in achieving its objectives.

The performance measurements used in this work were accuracy (Ac), sensitivity (Se), specificity (Sp), average false positives per image (FPI), average false negatives per image (FNI), overlay index (Ov) and area under the ROC curve (AUC).

The overlay index (Ov) indicates the average proportion of the size of the located areas related to the actual areas. If it is greater than one, this means that, on average, the located areas are larger than the original ones. If it is lower than 1, this means that, on average, the located areas are smaller than the original ones. It is computed by:

$$Ov = \frac{\sum_{i=1}^n \frac{Ns_i}{Nr_i}}{n} \quad (5)$$

where  $Ns_i$  is the number of pixels of the selected area in the image  $i$ ,  $Nr_i$  is the number of pixels of the area marked by the specialist in the image  $i$ , and  $n$  is the number of images where masses were found.

## 4. Results and discussion

To evaluate the mass detection methodology proposed in this work, several tests were performed. This section presents and discusses the results obtained by the various approaches used.

Initially, we randomly selected 623 images with only one mass from the DDSM. From those images, the stage of segmentation of regions of interest yielded a total of 3871 regions suspect of representing abnormalities, with 566 masses and 3305 non-masses. This segmentation stage was evaluated by verifying whether the region in the mammogram associated with the mass had any intersection with one of the suspect regions detected by the algorithm.

In 57 images from the sample, the segmentation process failed to include the masses in the set of regions of interest, representing 9.15% of the cases. This fact suggests that the parameters used in the templates should be optimized to achieve better segmentation performance.

The 566 masses that were correctly segmented represent 90.85% of the cases. These results demonstrate that the segmentation stage has good sensitivity, but produces many false positives – more precisely, 5.3 per image (3305 regions that do not contain masses, segmented as regions of interest in the 623 images) – which we expect to eliminate in the classification stage.

Tests were performed with and without the reduction of features, aiming to analyze the behavior of the classification. In this stage, the segmented candidates (566 masses and 3305 non-masses) were divided into 10 groups. This division has the objective of using the leave-N-out technique, whereby all groups are trained and tested to avoid biased tests. In each group, the number of support vectors needed to create the decision surface was recorded based on the training. At best, an average of 198 vectors was needed for the mass class and 1549 for the non-mass class. Thus, approximately one third

of the training data were used as support vectors. At worst, an average of 299 vectors was used for the mass class and 2606 vectors for the non-mass class. The selection of candidates in each group was performed randomly from the total number of segmented regions. The following subsections describe each of these approaches and discuss the obtained results.

### 4.1. Tests without reduction of variables

In the first testing approach, shape and texture features were used to describe the regions to be classified as masses or non-masses, as discussed in the preceding sections. Table 1 shows the average results obtained by the leave-N-out method with 10 groups. Initially, each descriptor was used separately, with the objective of analyzing the behavior of each descriptor without being influenced by the others. As Moran's and Geary's indexes have the same objective (to measure spatial correlation), a new test was performed combining both of them.

We can see in Table 1 that the analysis through Ripley's K function has higher sensitivity (87.25%), but presents low specificity (56.01%). Moran's and Geary's indexes, when used separately, have low performance; however, when combined, they yield a better overall performance.

It is important to observe that the overlay index (Ov) seems to present low performance, but we must emphasize that when specialists mark the area containing a mass in the mammogram, this area is usually larger than the actual mass. We can also note that the combination of Moran's and Geary's indexes has the largest area (AUC=0.792), while Moran's index, when used separately, has the smallest one (AUC=0.698).

Overall, the approach without feature reduction presented low performance regarding the classification of mass candidates. This occurs because some features are irrelevant, redundant or have high levels of noise. Other disadvantages of this approach are the time required to process the classification and the large amount of computer memory demanded, which imposes restrictions on larger combinations.

### 4.2. Tests with reduction of variables

In the second testing approach, the feature vectors were composed only by the features selected by the stepwise variable-reduction method, which yielded the following amounts: Shape, four features (eccentricity, circularity, compactness, circular density); Ripley's K function, 23 features (Table 2); Moran's index, 12 features (Table 3); Geary's index, seven features (Table 4).

Table 5 shows the average of the performance indicators obtained by the leave-N-out method with 10 groups. Each feature descriptor was analyzed separately as well as combined with others.

It can be observed in Table 5 that the combination of shape features and Moran's and Geary's indexes results in higher sensitivity (85.41%), but also in low specificity (85.41%). The best general performance is achieved by combining all features,

**Table 1**  
Results of tests on the proposed methodology without feature reduction.

Features	Se (%)	Sp (%)	Ac (%)	FPI	FNI	Ov	AUC
Shape	78.55	61.45	63.95	2.25	0.21	0.32	0.753
Ripley	87.25	56.01	60.58	2.57	0.13	0.306	0.738
Moran	75.65	55.32	58.29	2.61	0.24	0.381	0.698
Geary	69.36	63	63.93	2.16	0.31	0.392	0.704
Moran+Geary	78.57	70.17	71.43	1.74	0.21	0.362	0.792

**Table 2**  
Variables selected from Ripley's *K* function.

Quantization	Ring	Gray level
8	1	4, 7
16	0	0
	1	14
32	0	31
64	1	56, 58
128	0	0, 120, 127
	1	116, 127
256	0	193, 219, 235, 241, 242, 243, 253
	1	248, 249, 251, 252

**Table 3**  
Variables selected from Moran's index.

Quantization	Direction	Distance
8	90	2, 10
32	90	1
	135	5
64	135	4
128	90	2, 7
	135	6
256	0	1, 6
	135	8, 9

**Table 4**  
Variables selected from Geary's index.

Quantization	Direction	Distance
32	90	1, 4
	135	10
64	0	2, 4
128	0	10
256	135	1

**Table 5**  
Tests results with feature reduction. Caption: C, Feature combination; 1, Shape; 2, Ripley's *K* function; 3, Moran's index; 4, Geary's index.

Features	Se (%)	Sp (%)	Ac (%)	FPI	FNI	Ov	AUC
Shape (1)	77.64	62.15	64.42	2.21	0.22	0.32	0.753
Ripley (2)	81.23	68.5	70.37	1.84	0.19	0.30	0.803
Moran (3)	77.42	51.51	55.3	2.83	0.23	0.38	0.696
Geary (4)	70.66	61.99	63.25	2.22	0.29	0.39	0.708
C(1,2)	81.24	74.56	75.54	1.49	0.19	0.30	0.819
C(1,3)	83.39	67.42	69.75	1.9	0.17	0.33	0.792
C(1,4)	76.85	75.8	75.96	1.41	0.23	0.34	0.796
C(1,2,3)	79.64	79.61	79.62	1.19	0.2	0.32	0.85
C(1,2,4)	76.98	82.73	81.9	1.01	0.23	0.32	0.846
C(1,3,4)	85.41	75.1	77.07	1.42	0.15	0.32	0.846
<b>C(1,2,3,4)</b>	<b>80</b>	<b>85.68</b>	<b>84.62</b>	<b>0.84</b>	<b>0.2</b>	<b>0.32</b>	<b>0.87</b>
C(2,3,4)	81.75	81.86	81.86	1.06	0.18	0.32	0.861
C(3,4)	84.41	62.68	65.89	2.18	0.16	0.35	0.794

resulting in higher accuracy (84.62%) and larger area under the ROC curve (0.87).

The analysis using just texture presented good performance and a better balance between sensitivity (81.75%), specificity (81.86%) and accuracy (81.86%), as well as the second largest AUC (0.861). The analysis with poorest performance (line in italic) was obtained through Moran's index, which presents the smallest AUC (0.696) and the lowest accuracy (55.3%).

Comparing the items in Table 1 with their counterparts in Table 5, one can notice a slight increase in the average performance of the classifier. This fact is due to the removal of noise, redundancies and irrelevant items from the data, carried out by the stepwise feature-selection algorithm.

The approach with feature reduction allowed analyzing the classification based on the combination of features extracted from the candidates, with the advantage that it is a fast analysis does not require much memory to be processed. As one can notice in Tables 1 and 5, the overlay indexes were up to 0.4, indicating, in general that the objects classified as masses have smaller area than that informed in the DDSM. This fact is explained by the fact that specialists identify an area that is larger than the actual mass.

For the case studies described in the next section, we employed the combination of measurements (Table 5, line in bold), which showed the best balance between sensitivity and specificity, as shown in the AUC (0.87).

#### 4.3. Case studies

This section examines the stages of the proposed methodology by observing some test cases. The objective is to better illustrate the applied techniques and the processing flow as a whole, using the images generated at each stage.

Three cases will be examined. In the first case, the methodology fully succeeds in detecting the mass, that is, it achieved a good segmentation of the regions of interest and a correct classification of those regions. The second case studied is an example in which the methodology performed a good segmentation but failed to classify the segmented regions correctly. The third case presents a situation in which the methodology failed to segment the regions of interest adequately, affecting the final result even though the subsequent classification was performed satisfactorily.

##### 4.3.1. First case – correct detection

In the first case, the sequence of stages performed led to the correct detection of a mass in a mammography image. Fig. 10(a) shows the original image, such as it is available at the DDSM.

In the pre-processing stage, the image in Fig. 10(b) was produced. We can observe that the objects outside the breast were removed and we can see the effects of the histogram equalization performed to enhance the internal structures of the breast.

The first processing stage (Fig. 10(c)) performs the segmentation of the regions of interest through CNN using the Textutil and Blur templates.

In the following stage, features are extracted from the segmented regions of interest. This stage does not produce visual results, but a vector of values representing the extracted features. The next stage uses this vector to classify the regions of interest as masses or non-masses through a previously trained SVM. Fig. 10(d) shows, in blue, the region classified as mass.

To verify the success of the detection, the mark of the correct location of the mass, obtained from information contained in the DDSM, is printed in red on the resulting image.

##### 4.3.2. Second case – classification failure

The second case, presented in Fig. 11, shows the same sequence of steps described above, namely: original image (Fig. 11(a)); pre-processing result (Fig. 11(b)); selected candidates in blue (Fig. 11(c)); and the classification result, showing the region classified by the SVM as a mass in blue (Fig. 11(d)).

The marking in red indicates the correct location of the mass, obtained from information provided in the DDSM. As can be



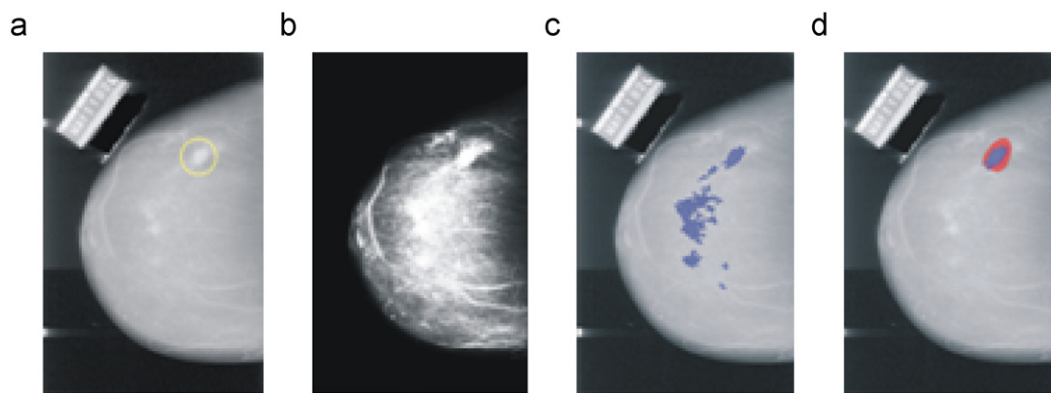


**Fig. 10.** Images of the first case study. (a) Original image. In yellow is the area containing the mass. (b) Pre-processed image. (c) In blue are the regions of interest selected during segmentation. (d) In blue is the mass detected by the methodology and in red is the area informed in the DDSM. (For interpretation of the references to color in this figure legend, the reader is referred to the web version of this article.)

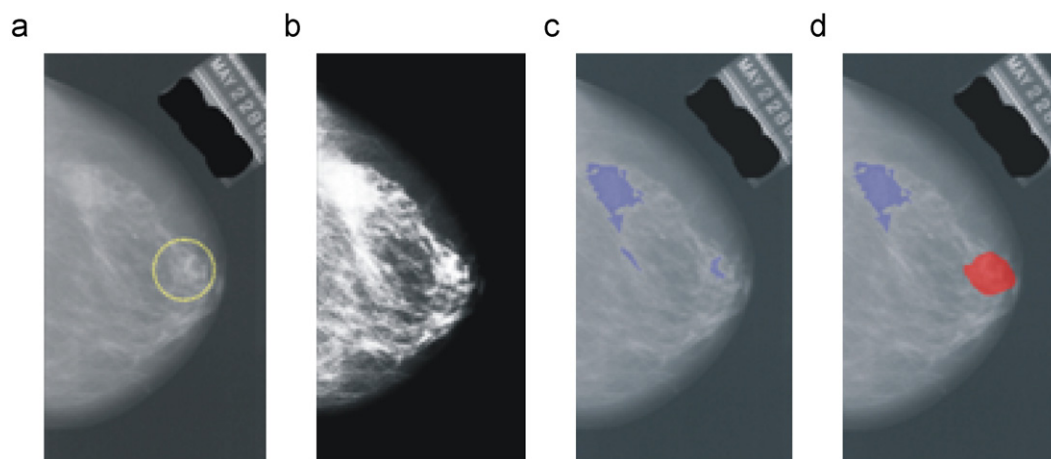


**Fig. 11.** Images of the second case study. (a) Original image. In yellow is the area containing the mass. (b) Pre-processed image. (c) In blue are the regions of interest selected during segmentation. (d) In blue is the candidate incorrectly selected as mass, and in red is the region containing a mass according to DDSM. (For interpretation of the references to color in this figure legend, the reader is referred to the web version of this article.)

observed in Fig. 11(c) and (d), even though the mass was segmented among the regions of interest, the classifier did not succeed in classifying it correctly, discarding it and presenting as mass a region that actually corresponds to normal breast tissue. Therefore, this case illustrates the occurrence of a false negative (mass classified as non-mass) and a false positive (non-mass classified as mass).

Among the possible factors related to this failure is the fact that the candidate selected as mass has a somewhat round shape. On the other hand, the candidate that actually corresponds to a mass has a longer and curved shape, which is probably why it was discarded. In this case, shape was considered more relevant than texture.

#### 4.3.3. Third case – segmentation failure

In the third case, the methodology fails to perform a correct segmentation.

Fig. 12 shows the images obtained during the processing, in the same order as the previous cases. In this case, the segmentation stage failed to include the mass among the regions of interest (Fig. 12(c)), as we can observe by the mark of the correct location of the mass, in red, in Fig. 12(d). So, although the classification stage was efficient in classifying all the segmented regions as normal tissue, the final result was affected, leading to a false negative.

The possible cause of the segmentation failure can be related to the size criterion established to consider a segmented region as a region of interest. That is, the region may have been segmented, but either it remained united to a large structure or the segmentation may have removed pixels in excess from the candidate, making it too small.

#### 4.4. Comparison with other studies

This section aims at drawing comparisons between the methodology proposed here and other methods to detect masses in mammograms, in order to put the quality of our work in perspective. It is important to stress that, for a fair comparison of the cited methodologies, it would be necessary to use the same images in all of the works. Besides, some parameters would need to be standardized, such as resolution, bits per pixels, etc. Another factor that should be equal is the sample used, for all the methodologies should use the same data for training and testing.

Table 6 presents a comparison among results of methods developed to detect masses in mammogram images.

The values informed for the methodology proposed here are those obtained through the analysis involving all of the descriptors (shape, Ripley's  $K$  function, and Moran's and Geary's indexes), which achieved the highest accuracy (84.62%), the smallest rate of false positives per image (0.84), the largest area under the ROC curve (0.827) and the highest specificity (85.68%).

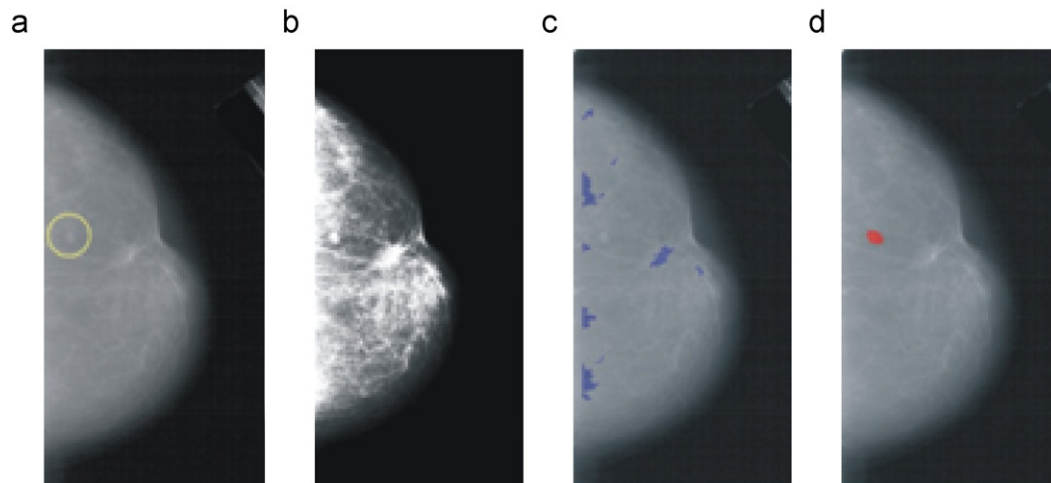


**Fig. 12.** Images of the third case study. (a) Original image. In yellow is the area containing the mass. (b) Pre-processed image. (c) Regions of interest selected during segmentation. (d) In red is the region containing a mass according to DDSM. (For interpretation of the references to color in this figure legend, the reader is referred to the web version of this article.)

**Table 6**

Comparison of methodologies for detection of masses.

Methods	Database	Se (%)	Sp (%)	Ac (%)	FPI	FNI	AUC	Ov
Nunes et al. [21]	DDSM	83.24	84.14	83.94	0.55	0.17	–	–
Martins et al. [20]	DDSM	–	–	89.3	0.93	0.02	–	–
Hassanien [9]	MIAS	–	–	98.46	–	–	–	–
Kom et al. [7]	Proprietary	95.91	–	–	–	–	0.946	–
Eltonsy et al. [6]	DDSM	81	–	–	0.6	–	–	–
Bellotti et al. [5]	MAGIC-5	82	–	–	2.8	–	0.862	–
Norbert et al. [4]	DDSM	95.1	–	–	4.3	–	–	–
Serhat et al. [3]	MIAS	81	–	–	0.33	–	–	–
Wang et al. [8]	DDSM	90.6	–	–	3.6	–	–	–
Timp et al. [31]	Proprietary	–	–	–	–	–	0.77	–
<b>Proposed method</b>	DDSM	80	85.68	84.62	0.84	0.2	0.87	0.325

Many of the cited works use sensitivity as a detection performance index. The proposed methodology achieved good sensitivity, of 88%. This index inversely affects the rate of false negatives per image (FNI), for which the proposed methodology achieved 0.2.

Most of the works do not use specificity as a performance measure. This does not allow us to know how many healthy tissues were incorrectly classified as masses. According to the information obtained, we can conclude that the sensitivity of the proposed methodology is an acceptable performance.

Through the comparison of false positives per image, we can observe that our methodology achieved a very good performance, because from the 3305 non-masses selected during the segmentation stage, only 473 were classified as masses, resulting in a rate of 0.84 false positives per image. Since this index is directly proportional to specificity, it allows us to deduct the specificity that is not informed in other works.

Regarding the AUC, we can notice that the proposed methodology achieved a good performance, of 0.87.

None of the other works used the overlay index; this means that further studies on segmentation techniques are necessary.

## 5. Conclusion

The results presented in Section 4 show that the methodology presented here achieved good performance. The step that segments the regions of interest segmented 566 from the 623 masses in the sample, or 90.85% of the cases. The classification of the segmented regions also obtained an acceptable performance, achieving 84.62% of

accuracy, 80% of sensitivity and 85.68% of specificity, with average rates of false positives per image and false negatives per image of 0.84 and 0.2, respectively, and AUC of 0.87.

Such results indicate that the combination of shape descriptors, Ripley's *K* function, and Moran's and Geary's indexes provides a good tool to characterize regions suspect of containing masses. Another important remark is the performance of the analysis involving only the texture descriptors (Ripley's *K* function and Moran's and Geary's indexes), which achieved an accuracy of 81.66%, sensitivity of 81.75% and specificity of 81.86%, with average rates of false positives and false negatives per image of 1.06 and 0.18, respectively, and an area under the ROC curve of 0.861.

Despite the good results obtained, several aspects of the methodology can be improved, allowing for even better results. One of these aspects is the performance of the segmentation stage, where nearly 9.15% of the original masses were lost.

We also observed that the objects classified as masses have areas smaller than the area informed by the DDSM (overlay index below 0.4, on average). This did not constitute a problem, but it indicates that larger masses can be divided into smaller ones, which might impact texture analysis, causing the mass to be classified as a false negative. Additional studies must be carried out to determine to what extent and how often this happens.

Another problem found in segmentation is the large number of regions of interest selected (566 regions containing masses and 3305 with healthy tissue). This numerical disproportion between the two classes ends up influencing the classifier, since much more information is available about one class in relation to the other. This has led to the need to use different weights for SVM training, in

order to reach a balance between sensitivity and specificity. A solution can be obtained through parameter optimization algorithms (genetic algorithms, fuzzy systems) to find a single template that can reduce the amount of false candidates and increase the proportion of masses found.

### Conflict of interest statement

None.

### Acknowledgments

The authors acknowledge CAPES, CNPq and FAPEMA for financial support.

## Appendix A. Shape features used in this work

### A.1. Eccentricity

The eccentricity ( $E$ ) measure defines how the structure is spatially distributed along its axis. It is calculated using central moment functions such as

$$E = \frac{(\mu_{02} - \mu_{20}) + 4\mu_{11}}{A} \quad (\text{A.1})$$

where  $A$  is the object area, and the central moment  $\mu$  can be calculated from

$$\mu_{pq} = \sum_{x=0}^{M-1} \sum_{y=0}^{N-1} (x-\bar{x})^p (y-\bar{y})^q \quad (\text{A.2})$$

where  $p+q > 1$  and represents the center of mass of the object.

### A.2. Circularity

Circularity ( $C$ ) shows how circular a certain object is. It is calculated by

$$C = \frac{4\pi A}{(p_{\text{convex}})^2} \quad (\text{A.3})$$

where  $A$  is the object area and  $p_{\text{convex}}$  is the perimeter of its convex hull.

### A.3. Compactness

The compactness ( $C_o$ ) measure indicates how dense the object is, compared to a perfectly dense shape: the circle. It is calculated by

$$C_o = \frac{p^2}{4\pi A} \quad (\text{A.4})$$

where  $A$  is the object area, and  $p$  is the perimeter.

### A.4. Circular disproportion

The circular disproportion can be obtained by

$$D = \frac{p}{2\pi R_e} \quad (\text{A.5})$$

where  $p$  is the perimeter of the object under study and  $R$  is the estimated radius of a circle with the same area as the object under

study. The estimated radius  $R_e$  can be obtained through

$$R_e = \sqrt{\frac{A}{\pi}} \quad (\text{A.6})$$

where  $A$  is the area of the object under study.

### A.5. Circular density

The circular density can be obtained by

$$D_e = \frac{100n}{A} \quad (\text{A.7})$$

where  $A$  is the area of the object,  $n$  is the total number of points belonging to the object, and the estimated circle of radius  $R$  can be obtained through

$$R_i = \frac{R_{\max}}{n} * i \quad \text{for } i = 1, \dots, n \quad (\text{A.8})$$

with center coinciding with in the center of mass of the object.

## References

- [1] N.C.I. (NCI), Cancer Stat Fact Sheets: Cancer of the Breast, available at <http://seer.cancer.gov/statfacts/html/breast.html>, 2010.
- [2] J.J. Fenton, S.H. Taplin, P.A. Carney, L. Abraham, E.A. Sickles, C. D'Orsi, E.A. Berns, G. Cutter, R.E. Hendrick, W.E. Barlow, J.G. Elmore, Influence of computer-aided detection on performance of screening mammography, *N. Engl. J. Med.* 356 (14) (2007) 1399–1409. doi:10.1056/NEJMoa066099. <http://content.nejm.org/cgi/content/abstract/356/14/1399>.
- [3] S. Özkes, O. Osman, A.Y. Çamurcu, Mammographic mass detection using a mass template, *Korean J. Radiol.* 6 (4) (2005) 221–228.
- [4] T. Norbert, P. Béla, Mass detection in mammograms combining two methods, in: Third European Medical and Biological Engineering Conference—EMBE05, International Federation for Medical and Biological Engineering, Czech Republic Prága, 2005, pp. 1–6.
- [5] R. Bellotti, F.D. Carlo, S. Tangaro, G. Gargano, G. Maggipinto, M. Castellano, R. Massafra, D. Cascio, F. Fauci, R. Magro, G. Raso, A. Lauria, G. Forni, S. Bagnasco, P. Cerello, E. Zanon, S.C. Cheran, E.L. Torres, U. Bottigli, G.L. Masala, P. Oliva, A. Retico, M.E. Fantacci, R. Cataldo, I.D. Mitri, G.D. Nunzio, A completely automated CAD system for mass detection in a large mammographic database, *Med. Phys.* 33 (8) (2006) 3066–3075.
- [6] N. Eltonsy, G. Tourassi, A. Elmaghraby, A concentric morphology model for the detection of masses in mammography, *IEEE Trans. Med. Imaging* 26 (6) (2007) 880–889 ISSN: 0278-0062, 10.1109/TMI.2007.895460.
- [7] G. Kom, A. Tiedeu, M. Kom, Automated detection of masses in mammograms by local adaptive thresholding, *Comput. Biol. Med.* 37 (1) (2007) 37–48 ISSN: 0010-4825, 10.1016/j.compbiomed.2005.12.004.
- [8] Y. Wang, X. Gao, J. Li, in: A Feature Analysis Approach to Mass Detection in Mammography Based on RF-SVM, *ICIP07*, 2007, pp. 9–12.
- [9] A. Hassani, Fuzzy rough sets hybrid scheme for breast cancer detection, *Image Vision Comput.* 25 (2) (2007) 172–183 ISSN: 0262-8856, http://dx.doi.org/10.1016/j.imavis.2006.01.026.
- [10] J. Suckling, J. Parker, D. Dance, S. Astley, I. Hutt, C. Boggis, et al., The mammographic images analysis society digital mammogram database, *Exerpta Med.* 1069 (1994) 375–378.
- [11] M. Heath, K. Bowyer, D. Kopans, Current Status of the Digital Database for Screening Mammography, *Digital Mammography*, Kluwer Academic Publishers, 1998, pp. 457–460.
- [12] C. Alonso-Montes, D.L. Vilarifiot, M.G. Penedo, CNN-based automatic retinal vascular tree extraction, in: Proceedings of Ninth IEEE International Workshop on Cellular Neural Networks and their Applications, I.C.S. Press, Piscataway, NJ, 2005, pp. 61–64.
- [13] A. Chernihovskiy, C. Elger, K. Lehnertz, Effect of inhibitory diffusive coupling on frequency-selectivity of excitable media simulated with cellular neural networks, in: Proceedings of Tenth IEEE International Workshop on Cellular Neural Networks and their Applications, I.C.S. Press, Piscataway, NJ, 2006, pp. 292–296.
- [14] D. Krug, H. Osterhage, E. Elger, K. Lehnertz, Estimating nonlinear interdependencies in dynamical systems using cellular nonlinear networks, *Phys. Rev.* 76 (2007) 201–220.
- [15] C. Rekeczky, Z.V.A. Tahy, T. Roska, CNN-based spatio-temporal nonlinear filtering and endocardial boundary detection in echocardiography, *Int. J. Circ. Theor. Appl.* 27 (1999) 171–207.
- [16] T. Szabo, P. Barsi, P. Szolgay, Application of analogic CNN algorithms in telemedical neuroradiology, in: Proceedings of Seventh IEEE International Workshop on Cellular Neural Networks and their Applications, World Scientific, Singapore, 2006, pp. 579–586.
- [17] P. Arena, A. Basile, M. Bucolo, L. Fortuna, Image processing for medical diagnosis using CNN, *Nucl. Instrum. Methods* 27 (2003) 174–178.

- [18] L.O. Chua, T. Roska, Cellular Neural Networks and Visual Computing: Foundations and Applications, Cambridge University Press, New York, NY, USA, 2002 ISBN 0-521-65247-2.
- [19] D. Costa, L.F. Campos, A.K. Barros, A.C. Silva, Independent component analysis in breast tissues mammograms images classification using LDA and SVM, *J. Comput. Biol. Med.* (2007) 231–234. doi:10.1109/ITAB.2007.4407389.
- [20] L. Oliveira Martins, A.C. Silva, A.C. De Paiva, M. Gattass, Detection of breast masses in mammogram images using growing neural gas algorithm and Ripley's *K* function, *J. Signal Process. Syst.* 55 (1–3) (2009) 77–90 ISSN: 1939-8018, <http://dx.doi.org/10.1007/s11265-008-0209-3>.
- [21] A.P. Nunes, A.C. Silva, A.C. de Paiva, Detection of masses in mammographic images using geometry, Simpson's Diversity Index and SVM, *Int. J. Signal Imaging Syst. Eng.* 3 (1) (2010) 43–51. doi:10.1504/IJSISE.2010.034631.
- [22] D.C. Pereira, M.Z. Nascimento, R.P. Ramos, R.D. Dantas, Automatic Detection of Breast Masses Using Two-View Mammography, in: World Congress on Medical Physics and Biomedical Engineering, Munich, Germany, 2009, pp. 917–920.
- [23] T. Soukup, I. Davidson, Visual Data Mining: Techniques and Tools for Data Visualization and Mining, John Wiley & Sons, Inc., New York, NY, USA, 2002 ISBN: 0471149993.
- [24] N.R. Pal, S.K. Pal, A review on image segmentation techniques, *Pattern Recognition* 26 (9) (1993) 1277–1294. doi:10.1016/0031-3203(93)90135-J ISSN: 0031-3203.
- [25] R.C. Gonzalez, R.E. Woods, Digital Image Processing, third ed., Addison-Wesley, Reading, MA, USA, 1992.
- [26] A. Zarandy, T. Roska, G. Liszka, J. Hegyesi, L. Kek, C. Rekeczky, Design of analogic CNN algorithms for mammogram analysis, in: Proceedings of the Third IEEE International Workshop on Cellular Neural Networks and their Applications, 1994, pp. 255–260, doi: 10.1109/CNNA.1994.381670.
- [27] G. Júnior, L. de Oliveira Martins, A. Silva, A. de Paiva, Computer-Aided Detection and Diagnosis of Breast Cancer Using Machine Learning Texture and Shape Features, first ed., IGI Global, 2010 (Chapter II).
- [28] L. Anselin, Computing environments for spatial data analysis, *Journal of Geographical Systems* 2 (2001) 201–220.
- [29] R.O. Duda, P.E. Hart, Pattern Classification and Scene Analysis, Wiley-Interscience Publication, New York, 1973.
- [30] J.T. Bushberg, A.J. Seibert, E.M. Leidholdt, J.M. Boone, The Essential Physics of Medical Imaging, second ed., Lippincott Williams & Wilkins, Philadelphia, PA, 2001.
- [31] S. Timp, C. Varela, N. Karssemeijer, Temporal change analysis for characterization of mass lesions in mammography, *IEEE Trans. Med. Imaging* 26 (7) (2007) 945–953.

**Edgar Moraes Diniz** received his M.Sc. degree in Computer Graphics in 2011 from Federal University of Maranhão. His primary research interest is Computer Graphics and Image Processing applied on Medicine. His academic production includes 3D data reconstruction and visualization, and surgery simulation.

**Aristófares Corrêa Silva** received a Ph.D. degree in Informatics from Pontifical Catholic University of Rio de Janeiro, Brazil in 2004. Currently he is a Professor at the Federal University of Maranhão (UFMA), Brazil. He teaches image processing, pattern recognition and programming language. His research interests include image processing, image understanding, medical image processing, machine vision, artificial intelligence, pattern recognition and, machine learning.

**Anselmo Cardoso de Paiva** received B.Sc. in civil engineering from Maranhão State University, Brazil in 1990, a M.Sc. in civil engineering, Structures and a Ph.D. in Informatics from Pontifical Catholic University of Rio de Janeiro, Brazil in 1993 and 2002. He is currently a Professor at the Informatics Department, Federal University of Maranhão, Brazil. His current interests include medical image processing, geographical information systems and scientific visualization.

**Marcelo Gattass** took his Ph.D. in 1982 from Cornell University and is a full professor at PUC-Rio's Computer Science Department. He currently teaches Computer Graphics and 3D Computer Vision for graduate students and Data Structures for undergraduates. He is also the Director of Tecgraf/PUC-Rio, Computer Graphics Technology Laboratory, where he supervises several industry-cooperation projects in the areas of 3D modeling and visualization, geographic information systems, user interfaces, and web-based applications.

**Wener Borges de Sampaio** received B.Sc. in Computer Science from Federal University of Piauí (UFPI), Brazil in 2005, a M.Sc. degree in Electric Engineering at the Federal University of Maranhão (UFMA), Brazil in 2009. His major interest nowadays is obtaining a Ph.D degree at the same university. His research interests include signals and image processing, pattern recognition and automation systems applied on medicine.